Journal of Alloys and Compounds 968 (2023) 172205

Contents lists available at ScienceDirect

Journal of Alloys and Compounds

journal homepage: www.elsevier.com/locate/jalcom

Effect of Gd substitution on structure, optical and magnetic properties, and heating efficiency of Fe_3O_4 nanoparticles for magnetic hyperthermia applications

Luu Huu Nguyen [a,b], Nguyen Hoai Nam [c], Le The Tam [d], Dinh Van Tuan [e], Nguyen Xuan Truong [c,f], Nguyen Van Quynh [g], Phan Thi Hong Tuyet [d], Ha Phuong Thu [c], Do Hung Manh [c], Pham Thanh Phong [a,b], Pham Hong Nam [c,f,*]

[a] Laboratory of Magnetism and Magnetic Materials, Science and Technology Advanced Institute, Van Lang University, Ho Chi Minh City, Vietnam
[b] Faculty of Applied Technology, School of Technology, Van Lang University, Ho Chi Minh City, Vietnam
[c] Institute of Materials Science, Vietnam Academy of Science and Technology, 18 Hoang Quoc Viet, Cau Giay, Hanoi, Vietnam
[d] Vinh University, 182 Le Duan, Vinh City, Vietnam
[e] Electric Power University, 235 Hoang Quoc Viet, Bac Tu Liem, Hanoi, Vietnam
[f] Graduate University of Science and Technology, Vietnam Academy of Science and Technology, 18 Hoang Quoc Viet, Cau Giay, Hanoi, Vietnam
[g] University of Science and Technology of Hanoi (USTH), Vietnam Academy of Science and Technology, 18 Hoang Quoc Viet, Cau Giay, Hanoi, Vietnam

ARTICLE INFO

Keywords:
Gd substitution
Fe_3O_4
Magnetic properties
Optical properties
Magnetic inductive heating

ABSTRACT

This work presents the synthesis of $Fe_{3-x}Gd_xO_4$ nanoparticles and the investigation of the impact of Gd content (x) on structural characteristics of nanoparticles, including lattice parameters, crystallite size, and X-ray density. The high-resolution images of Transmission Electron Microscopy reveal that the synthesized $Fe_{3-x}Gd_xO_4$ nanoparticles have a narrow distribution in size statistics between 9 and 12.5 nm. Interestingly, analyzing different prepared samples reveals that both the saturation magnetization and magnetic anisotropy decrease simultaneously with the increase of band gap while remaining independent of the specific absorption rate (*SAR*) value. The *SAR* is greater than that of pure Fe_3O_4 nanoparticles. In a specific case of $Fe_{2.75}Gd_{0.25}O_4$ sample where the optimal value of x is 0.25, the highest *SAR* value obtained is 237.4 W/g. Besides, the experimental results demonstrate an optimal doping content with the highest *SAR* value of $Fe_{2.75}Gd_{0.25}O_4$ nanoparticles along with the theoretical explanation by analyzing the Linear Theory Response framework based on the relationship between magnetic anisotropy and diameter with *SAR* value. The theoretical and experimental evidence fully demonstrate that doping is an effective approach for optimizing as-synthesized NPs to enable efficient hyperthermia applications.

1. Introduction

Magnetic iron oxide nanoparticles (NPs) exhibits some specific properties which make them a potential candidate for a wide range of applications [1,2]. Among them, the γ-Fe_2O_3 and spinel ferrites NPs are widely studied due to their unique magnetic properties and biocompatibility [3–7]. For instance, Fe_3O_4 NPs; γ-Fe_2O_3 NPs [8]; $CoFe_2O_4$ [9] and $MnFe_2O_4$ [10] NPs have been proved as the promising candidates for hyperthermia applications. Under specific stimulating condition within a short time period, those stimulated NPs could generate sufficient heat for hyperthermia treatment application. Interestingly, the Fe_3O_4 NPs at low concentrations between 0.1 and 10 μg/mL were demonstrated no toxicity effects [2]. As a result, the Fe_3O_4 NPs have been most frequently employed in biological applications, such as cancer therapy based on Magnetic Inductive Heating (MIH), acting as a contrast agent of Magnetic resonance imaging (MRI), and as a magnetic platform for targeted drug delivery [2,11,12].

For an efficient exploit of magnetic properties of Fe_3O_4 NPs in biomedical applications, several approaches to synthesize NP of different configurations have been proposed such as core-shell structure NPs [13–15], substitution or doping of NPs [16–18], and hard/soft or soft/hard ferrite nanocomposites [19,20].

* Corresponding author at: Institute of Materials Science, Vietnam Academy of Science and Technology, 18 Hoang Quoc Viet, Cau Giay, Hanoi, Viet Nam.
E-mail addresses: luuhuunguyen@vlu.edu.vn (L.H. Nguyen), namph.ims@gmail.com (P.H. Nam).

https://doi.org/10.1016/j.jallcom.2023.172205
Received 27 April 2023; Received in revised form 12 September 2023; Accepted 15 September 2023
Available online 16 September 2023

Among them, the substitution or doping of pristine NPs is a relatively facile approach, particularly for Fe_3O_4 NPs or other spinel ferrite NPs. Interestingly, it has been found that by doing technique, the characteristics such as the material structure and its magnetic properties are influenced by the doped cations and its distribution over tetrahedral and octahedral sites [2]. Therefore, doping (substitution) other ions to spinel ferrites NPs generates different structures with flexible magnetic properties [21,22]. Recently, many scientists have focused on the synthesis of $Fe_{3-x}M_xO_4$ (M = Co, Mn, Zn, Gd …) NPs for their potential use in MIH and MRI [23–30]. This is due to these nanoparticles might exhibit the promising results in improving their efficiency of these mentioned applications. It also have been reported that the doped Fe_3O_4 NPs can be used as a dual contrast agent of MRI [24]. For MIH applications, J. Giri et al. reported that specific absorption rate (*SAR*) of $Fe_{1-x}Mn_xFe_2O_4$ NPs ($x \leq 0.4$) was higher than that of Fe_3O_4 NPs due to an increase of saturated magnetization [26]. In other research, E. Fantechi et al. generated 8 nm of $Co_xFe_{3-x}O_4$ NPs, with a SAR value varies from 10 to 40 W/g, which are always higher than that of Fe_3O_4 NPs (6.5 W) /g) in the same conditions [27]. These findings are in line to many similar previous works [28–30]. As a consequence, it is no doubt to conclude that the substitution of Fe^{3+} (or Fe^{2+}) ions in Fe_3O_4 NPs by other ions has been an efficient approach to enhancing its *SAR* value for hyperthermia applications.

Among potential dopants, Gd^{3+} ion was well-known as the traditional contrast agents of MRI [24]. It is also used to increase the efficiency of magnetic NPs in hyperthermia applications [31]. For instance, K. P. Hazarika et al. reported that the Gd-doped Fe_3O_4 NPs had a *SAR* value that was larger than that of pure Fe_3O_4 NPs [31]. Besides, D. Jaison et al. observed the existence of optimal content of Gd substitution of $CoGd_xFe_{2-x}O_4$ NPs for their SAR values [18]. However, the previous works mentioned also found the reduction of SAR value when doping Gd^{3+} ions to Fe_3O_4 NPs [24] or γ-Fe_2O_3 NPs [16] in spite of the doped samples were still promising candidates for hyperthermia applications. The combination of Gd^{3+} ions and spinel ferrites NPs caused interesting-conflict results. Noting that the *SAR* value of NPs depends on various parameters of NPs such as particle size, size distribution, particle shape, saturation magnetization (M_S), coercivity, magnetic anisotropy (*K*), intra-particle and inter-nanoparticle interactions [32–34]. In particular, the proportional relationship between M_S and *SAR* [33] was suitably used to explain the reduction of *SAR* in the works of I. Alotaibi et al. [16] or N. D. Thorat et. al [24]. In contrast, this relationship also led to unexplained results in References [18,31]. In the work of K. P. Hazarika et al., the authors focus the enhancement of *SAR* with an increase of Gd^{3+} concentration in the doped samples, but the reduction of M_S caused the fall off *SAR* value. The work of D. Jaison et al. [18] also revealed some strange results regarding the relationship between *SAR* and M_S. Currently, the SAR value of the doped sample reached the maximal value at x = 0.24. Until now, only few works [16,18,30,31] have experimentally proved the influence of Gd^{3+} doped concentration on its *SAR* value without using any theoretical models to explain the obtained results.

This work focuses on both experimental and theoretical explanations of the effect of Gd^{3+} ions substitution for Fe^{3+} ions on the SAR value of the $Fe_{3-x}Gd_xO_4$ (x = 0.0; 0.05; 0.1; 0.15; 0.2; 0.25; and 0.3) NPs that were synthesized by the co-precipitation method. The relationship between the concentration of Gd^{3+} dopant with structural parameters, band gap value (E_g), saturation magnetization (M_S), and magnetic anisotropy (K) have been evaluated to study the theoretical SAR value. The theoretical results indicate the existence of the SAR peak value at critical magnetic anisotropy. Besides, the experimental results demonstrate an optimal doping content with highest SAR value of $Fe_{2.75}Gd_{0.25}O_4$ nanoparticles along with the theoretical explanation by analyzing the Linear Theory Response (LRT) framework based on the relationship between K and D values with SAR value. The theoretical and experimental evidences fully demonstrate that doping is an effective approach for optimizing as-synthesized NPs to enable efficient hyperthermia applications.

2. Experimental detail

2.1. Chemical

The Sigma-Aldrich chemicals including Iron(II) chloride tetrahydrate ($FeCl_2{\cdot}4H_2O$, purity ≥ 98 %), Iron(III) chloride hexahydrate ($FeCl_3{\cdot}6H_2O$, purity ≥ 98 %), and Gadolinium(III) chloride hexahydrate ($GdCl_3{\cdot}6H_2O$, purity ≥ 97 %) with sodium hydroxide (NaOH) were used for the fabrication of $Fe_{3-x}Gd_xO_4$ (x = 0.0, 0.05, 0.1, 0.15, 0.2, 0.25, and 0.3) NPs. Besides, the double distilled water was used for all experiments in this work.

2.2. Sample preparation

The $Fe_{3-x}Gd_xO_4$ (x = 0.0, 0.05, 0.1, 0.15, 0.2, 0.25, and 0.3) NPs were synthesized by the co-precipitation method, which corresponded to Fe_3O_4, $Fe_{2.95}Gd_{0.05}O_4$, $Fe_{2.9}Gd_{0.1}O_4$, $Fe_{2.85}Gd_{0.15}O_4$, $Fe_{2.8}Gd_{0.2}O_4$, $Fe_{2.75}Gd_{0.25}O_4$, and $Fe_{2.7}Gd_{0.3}O_4$ samples, respectively. Firstly, a mixture solution was prepared by dissolving 3.184 g $FeCl_2$.4 H_2O and mg (m = 8.641 g, 8.722 g, 8.803 g, 8.885 g, 8.966 g, 9.048 g and 9.129 g) g of a mixture of $FeCl_3$.6 H_2O and $GdCl_3{\cdot}6H_2O$ in 20 mL double distilled water, and stirring for an hour at room temperature. Then, adding 50 mL of NaOH solution (2 M) at 80 ^oC to the as-prepared mixture while it was agitating at 500 rpm for 60 min. Consequently, the pH of the obtained solution was approximately of 12 (pH ≈ 12). Subsequently, the prepared solution was kept at a temperature of 80 ^oC for 60 min, before cooling it naturally down to room temperature. The double distilled water was used to wash the solution twice in order to the its final pH value was around of ≈ 7. The precipitates were then collected by a magnet, and were dried at 60 °C for 300 min. Finally, the $Fe_{3-x}Gd_xO_4$ (x = 0.0, 0.05, 0.1, 0.15, 0.2, 0.25, and 0.3) NPs were obtained.

2.3. Characterization

The crystallographic structures, phase identification, and sample purity of the $Fe_{3-x}Gd_xO_4$ NPs were analyzed by X-ray diffraction (XRD) equipment with a Bruker D8-Advance instrument, in the reflection mode a Cu-Kα line of 1.5406 Å. The normal elemental compositions of $Fe_{3-x}Gd_xO_4$ NPs were revealed by the Energy Dispersive X-ray Spectroscopy (EDX) analysis on the Hitachi S-4800 FESEM equipped. The high-resolution Transmission Electron Microscopy (TEM) (JEOL JEM-1010 system operating at 120 kV) was used to observe the morphology, and calculate the average nanoparticle size of all dried samples. All Raman spectra of samples were collected via the Jobin-Yvon Lab RAM HR800 Raman Spectrometer, equipped with a laser of 532 nm wavelength source at power of 10 mW. The optical absorbance of all samples was obtained by a Cary 5000 UV–Visible–NIR double beam spectrophotometer (Agilent Technologies, Santa Clara, USA) over the range of 300–800 nm wavelength. The UV–visible spectroscopic studies were presented in details in Supporting information [35–39]. The DC magnetic properties of the samples were investigated at room temperature by a homemade vibrating sample magnetometer under the magnetic field up to11 kOe (≈ 875.4 kA/m). The magnetic induction heating rates of the $Fe_{3-x}Gd_xO_4$ NPs were measured using a commercially available UHF-20A, supplied by Chengdu JinKeZhi Electronic Co, Ltd, at the frequency of 450 kHz and amplitude of 100 – 300 Oe (≈ 8 – 24 kA/m). The value of *SAR* was computed using the following equation [40]:

$$SAR(W/g) = \frac{C}{m}\frac{dT}{dt} \quad (1)$$

where m is the concentration (mg/mL) of sample in magnetic fluid, C is the specific heat capacity of water (4.185 J/gK), and dT/dt is the slope of

the measured temperature-time curve. In the current experiments, the temperature slope was calculated via analyzing the temperature versus time curves for the whole time range, i.e. first to fit experimental curves by the following equation [40]:

$$T = T_p + \Delta T\left(1 - e^{t/t_m}\right) \quad (2)$$

to gain: ΔT, t_m are the temperature difference between the initial and steady state, and the time constant of heating, respectively. Then, the value of dT/dt is determined as equal to $\Delta T/t_m$.

The outcomes of these measurements will be discussed in depth in the results and discussion sections.

3. Results and discussion

3.1. XRD studies

Fig. 1 presents the experimental XRD patterns of $Fe_{3-x}Gd_xO_4$ ($x = 0.0, 0.05, 0.1, 0.15, 0.2, 0.25$, and 0.3) NPs, which were measured at ambient temperature. Fig. 2 displays the Rietveld refinement results of Fe_3O_4 and $Fe_{2.75}Gd_{0.25}O_4$ samples. As can be seen in Fig. 2(a), there are seven characteristic diffraction peaks at 2θ values of 30.066°, 35.592°, 37.044°, 43.038°, 53.391°, 56.914° and 62.496° for the Fe_3O_4 sample. These peaks were attributed to the crystal plane of (220), (311), (400), (422), (511), (440), and (533) of cubic spinel (Fd3m) structured Fe_3O_4 (the JCPDS card no. 85–1436 [40]). Thus, it fully demonstrates the unique phase existed for the Fe_3O_4 sample. The other XRD patterns of the $Fe_{3-x}Gd_xO_4$ ($x \neq 0$) samples exhibit prominent (*h,k,l*) planes indexed by (220), (311), (400), (511), and (440) (Fig. 1a), corresponding to the formation of the single crystallographic phase of Fe_3O_4. In addition, other crystalline phases' diffraction peaks were not found for these samples in Fig. 1(a). However, it confirms the existence of a secondary phase is observed in previous works related to doping samples of spinel ferrites NPs. For instance, B. Aslibeiki et al. found the Ag phase for Ag-doped $MnFe_2O_4$ NPs [41]. Similarly, X. Koutsoumbou et al. found that the secondary phase for Rare earth (Dy, Yd, Gd)-doped $CoFe_2O_4$ NPs [30]. Interestingly, F. Javed et al. found that the Gd phase for Gd-doped $CoFe_2O_4$ NPs when the content of Gd substitution was 0.5. The content of Gd^{3+} ions was 0.25, a secondary phase has not presence [23]. In contrast, S. A. Jadhav et al. was unsuccessful to prove the existence of the Gd phase for Gd-doped mixed Ni-Cu-Zn ferrites [17]. All results cited reveal that the existence of secondary phase depends strongly on fabrication methods and materials. At the highest content of Gd ($x = 0.3$) in this work, the Rietveld refinement findings indicated the existence of all typical diffraction peaks, which are similar to the results of the Fe_3O_4 sample. As a result, all samples have a unique single crystallographic phase of Fe_3O_4. Therefore, it demonstrates the successful synthesis of $Fe_{3-x}Gd_xO_4$ NPs.

The (311) plane is the strongest reflection representing for the spinel phase of all samples (Fig. 1a). As demonstrated seen in Fig. 1(b), the reduction of 2θ value corresponding to the (311) planes is found with an increase in the number of Gd^{3+} ions, indicating a left shift peak. This trend could be caused by the replacement of Fe^{3+} ions by Gd^{3+} ions in Fe_3O_4 NPs. The similarly tendency is also observed in other diffraction peaks. In fact, for a small amount of Gd^{3+} ions doping with Fe_3O_4 ($x \leq 0.3$) in this work, the complete replacement of Fe^{3+} ions by Gd^{3+} ions leads to the creation of the $Fe_{3-x}Gd_xO_4$ ($x \neq 0$) samples with the single crystallographic phase of Fe_3O_4. The evidence for this is the presence of characteristic diffraction peaks in the $Fe_{3-x}Gd_xO_4$ ($x \neq 0$) samples. Thus, this replacement causes the reduction of 2θ value corresponding to the (311) planes for doped samples as compared with Fe_3O_4 samples. On the other hand, the completion of these replacements leads to the systematic reduction of the 2θ value with an increase of Gd^{3+} ions in the $Fe_{3-x}Gd_xO_4$ ($x \neq 0$) samples (Fig. 1b). Additionally, as a result of this left shift of the (311) diffraction peak, the value of structural parameters changes with an increase of Gd content in the $Fe_{3-x}Gd_xO_4$ NPs. This is good in agreement with our results of the experimental lattice parameter (*a*) and crystallite size (D_{XRD}) (Table 1). They are computed using the following equations [42]:

$$a = d_{hkl} \quad \sqrt{h^2 + k^2 + l^2} \quad (1)$$

$$D_{XRD} = \frac{0.9\lambda}{\beta\cos\theta} \quad (2)$$

in which, (*h,k,l*) are the Miller indices, d_{hkl} is the inter-planar spacing, λ is the wavelength of the Cu-Kα radiation, θ is the Bragg angle, and β is the full-width at half-maximum (FWHM) of (311) peaks. In addition, the X-ray density (ρ_{XRD}) of the $Fe_{3-x}Gd_xO_4$ NPs could be calculated using this formula [42]:

$$\rho_{XRD} = \frac{8M}{N_A a^3} \quad (3)$$

where M is the molecular weight of each sample and N_A is Avogadro's number. All value of *a*, D_{XRD}, and ρ_{XRD} of the $Fe_{3-x}Gd_xO_4$ NPs were presented in Table 1.

As above mentioned, the left shift of the (311) peaks of the $Fe_{3-x}Gd_xO_4$ NPs leads to the changing of structural parameters. Table 1 shows that the value of lattice parameter (*a*) increased from 8.359 Å (Fe_3O_4) to 8.391 Å ($Fe_{2.7}Gd_{0.3}O_4$) with an increase of Gd^{3+} ions in the $Fe_{3-x}Gd_xO_4$ NPs. Similarly, N. D. Thorat et al. found an increase of *a* value in the range from 8.373 Å to 8.446 Å when the content of Gd^{3+} ions increased [24]. This tendency was also observed in the work of K. P. Hazarika et al. [31]. In addition, this trend was also detected for the combination of Gd^{3+} ions and spinel ferrite NPs in the previous works [23,30,43,44]. It is clear that the bigger radius of Gd^{3+} ions (0.94 Å [24]) as that of Fe^{3+} ions (0.645 Å [24]) led to the increase of *a* value. Table 1 also indicated an increase in ρ_{XRD} value with an increase in the

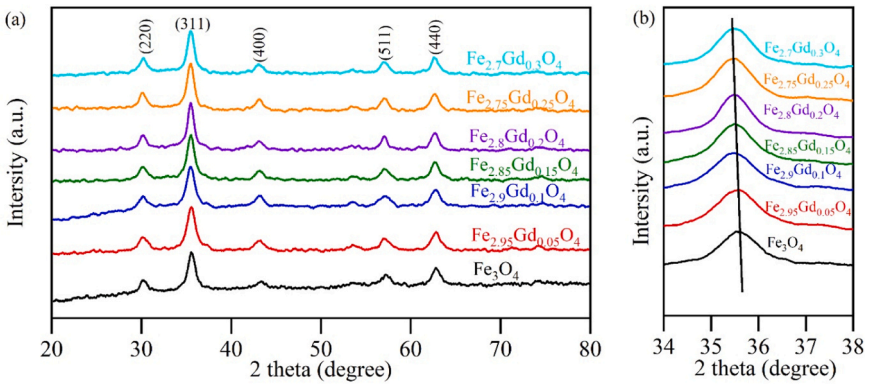

Fig. 1. (a) XRD patterns and (b) (311) diffraction peak of $Fe_{3-x}Gd_xO_4$ NPs.

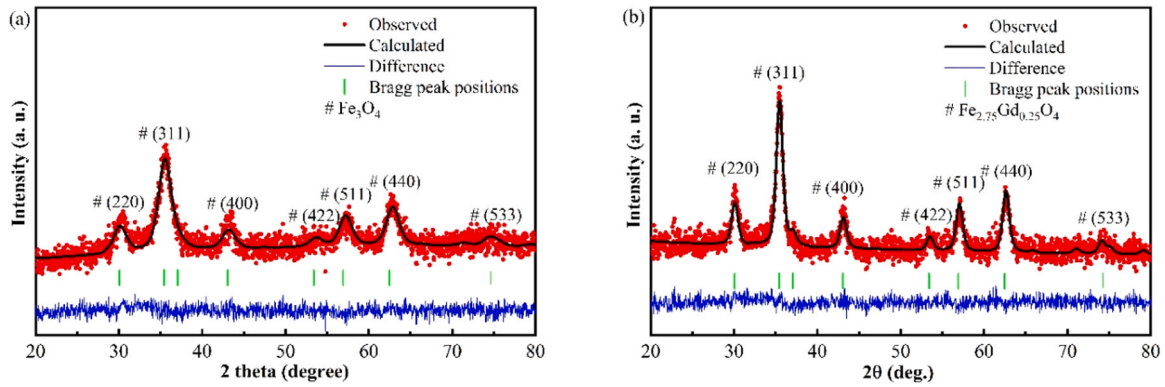

Fig. 2. Refined X-ray diffraction patterns of (a) Fe_3O_4 and (b) $Fe_{2.75}Gd_{0.25}O_4$ samples.

Table 1
Lattice parameter (a), crystallite size (D_{XRD}), X-ray density (ρ_{XRD}), and D_{TEM} values of $Fe_{3-x}Gd_xO_4$ NPs.

Sample	a (Å)	D_{XRD} (nm)	ρ_{XRD} (g/cm^3)	D_{TEM} (nm)
Fe_3O_4	8.359 ± 0.001	8.5 ± 0.1	5.28 ± 0.05	9.0 ± 1.0
$Fe_{2.95}Gd_{0.05}O_4$	8.369 ± 0.001	7.6 ± 0.1	5.37 ± 0.05	9.5 ± 0.5
$Fe_{2.9}Gd_{0.1}O_4$	8.384 ± 0.001	7.6 ± 0.1	5.46 ± 0.05	9.5 ± 0.5
$Fe_{2.85}Gd_{0.15}O_4$	8.385 ± 0.001	8.3 ± 0.1	5.57 ± 0.05	10.0 ± 1.0
$Fe_{2.8}Gd_{0.2}O_4$	8.386 ± 0.001	8.5 ± 0.1	5.68 ± 0.05	11.0 ± 1.0
$Fe_{2.75}Gd_{0.25}O_4$	8.389 ± 0.001	8.7 ± 0.1	5.79 ± 0.05	12.5 ± 0.5
$Fe_{2.7}Gd_{0.3}O_4$	8.391 ± 0.001	8.9 ± 0.1	5.90 ± 0.05	12.5 ± 0.5

number of Gd^{3+} ions could be attributed to the rise of the a value in the $Fe_{3-x}Gd_xO_4$ NPs.

For the tendency of crystallite size of the $Fe_{3-x}Gd_xO_4$ NPs, there is little difference as compared to the trend of lattice parameter or X-ray density value. As can be seen Eq. (2), the value of D_{XRD} are computed based on the value of FWHM and cosθ at (311) peaks of each sample. The D_{XRD} value depends on not only the left shift of the (311) peak but also the broad of this peak. At $x = 0.05$, this broadening of the (311) peak leads to the smaller value of D_{XRD} for $Fe_{2.95}Gd_{0.05}O_4$ sample (7.6 nm) as compared to that of Fe_3O_4 sample (8.5 nm). For $Fe_{3-x}Gd_xO_4$ NPs with $x \neq 0$, an increase of D_{XRD} value with an increase of x content is found (Table 1). K. P. Hazarika et al. found that the crystallite size changed from 13.2 nm to 14.06 nm when number of Gd^{3+} ions increased [31]. The similarly result was reported in previous work of N. D. Thorat et al. [24]. However, a decrease, increase or almost unchanging crystallite size was observed for the combination of Gd and other spinel ferrites other previous works [16,23,30,43,44]. Recently, K. P. Hazarika et al. explained this issue based on the competition in the replacement Fe^{2+}/Fe^{3+} ions (tetrahedral/ octahedral sites of iron) by Gd^{3+} ions [31]. Noting that when Gd^{3+} ions were doped in γ-Fe_2O_3 NPs, the replacement Fe^{3+} ions by Gd^{3+} ions led to the increase of crystallite size of doped samples as compared with pure γ-Fe_2O_3 NPs [16]. When Gd^{3+} ions were doped in Fe_3O_4 NPs, the crystallite size of doped samples might be decreased, increased or almost unchanged [16,23,30,43,44] because of the competition at tetrahedral and octahedral sites [31]. All results indicated that the changing of D_{XRD} value depended on the difference of Gd^{3+} ions with ions, which were replaced by them.

Next, using the following equations (Eqs. (4)–(10)) [42] with the u value (0.381 Å) of the oxygen positional parameter, and lattice parameter (a) of each sample, the calculation results of the hopping length (L_A and L_B), tetrahedral bond length (d_{AO}), octahedral bond length (d_{BO}), tetrahedral edge length (d_{AOE}), shared octahedral edge length (d_{BOE}), and unshared octahedral edge length (d_{BOEU}) are presented in Table 2.

$$L_A = 0.25a\sqrt{3} \tag{4}$$

$$L_B = 0.25a\sqrt{2} \tag{5}$$

$$d_{AO} = a\sqrt{3}\left(u - \frac{1}{4}\right) \tag{6}$$

$$d_{BO} = a\left(3u^2 - \frac{11}{4}u + \frac{43}{64}\right)^{1/2} \tag{7}$$

$$d_{AOE} = a\sqrt{2}\left(2u - \frac{1}{2}\right) \tag{8}$$

$$d_{BOE} = a\sqrt{2}(1 - 2u) \tag{9}$$

$$d_{BOEU} = a\left(4u^2 - 3u + \frac{11}{16}\right)^{1/2} \tag{10}$$

Noting that all of the above seven parameters increases with an increase in the x value of the $Fe_{3-x}Gd_xO_4$ NPs as a general trend (Table 2). This phenomenon is attributed to the enhancement in lattice expansion caused by the substitution of the small radius ions for large radius ions. For example, S. B. Somvanshi et al. observed the increase of above seven parameters with an increase of doping content for $Zn_{0.5}Mg_{0.5}Fe_{2-x}Gd_xO_4$ NPs [43]. In contract, the decrease of these parameters with an increase of doping content for $NiAl_xCr_xFe_{2-2x}O_4$ NPs, which related to the substitution of the large radius ions for small radius ions [21]. Noting that the radius of Gd^{3+} ions were larger than that of Fe^{3+} ions; thus, the general tendency of these parameters seems to be related to the Gd substitution in these doped samples. These tendencies were similar with previous works [21,22,43,45].

Table 2
The value of L_A, L_B, d_{AO}, d_{BO}, d_{AOE}, d_{BOE}, and d_{BOEU} of the $Fe_{3-x}Gd_xO_4$ NPs.

Sample	L_A (Å)	L_B (Å)	d_{AO} (Å)	d_{BO} (Å)	d_{AOE} (Å)	d_{BOE} (Å)	D_{BOEU} (Å)
Fe_3O_4	3.620 ± 0.002	2.955 ± 0.002	1.897 ± 0.001	2.041 ± 0.001	3.097 ± 0.002	2.813 ± 0.002	2.957 ± 0.002
$Fe_{2.95}Gd_{0.05}O_4$	3.624 ± 0.002	2.959 ± 0.002	1.899 ± 0.001	2.043 ± 0.001	3.101 ± 0.002	2.817 ± 0.002	2.961 ± 0.002
$Fe_{2.9}Gd_{0.1}O_4$	3.630 ± 0.002	2.964 ± 0.002	1.902 ± 0.002	2.047 ± 0.002	3.106 ± 0.002	2.822 ± 0.002	2.966 ± 0.002
$Fe_{2.85}Gd_{0.15}O_4$	3.631 ± 0.002	2.965 ± 0.003	1.903 ± 0.002	2.047 ± 0.002	3.107 ± 0.002	2.822 ± 0.002	2.966 ± 0.002
$Fe_{2.8}Gd_{0.2}O_4$	3.631 ± 0.002	2.965 ± 0.003	1.903 ± 0.002	2.047 ± 0.002	3.107 ± 0.002	2.823 ± 0.002	2.967 ± 0.002
$Fe_{2.75}Gd_{0.25}O_4$	3.633 ± 0.003	2.966 ± 0.004	1.903 ± 0.002	2.048 ± 0.002	3.108 ± 0.003	2.824 ± 0.003	2.968 ± 0.003
$Fe_{2.7}Gd_{0.3}O_4$	3.633 ± 0.003	2.967 ± 0.004	1.904 ± 0.002	2.049 ± 0.002	3.109 ± 0.003	2.824 ± 0.003	2.968 ± 0.003

3.2. TEM analysis

Fig. S1 presents the TEM images of the $Fe_{3-x}Gd_xO_4$ NPs. The histograms of the size distributions and the average nanoparticle sizes, D_{TEM} determined from TEM images for each sample are also inset in Fig. S1. The solid lines in the inset of each sample is a good fit for data using the lognormal distribution (Eq. (11)) [40]. As can be seen in Fig. S1, the value of D_{TEM} are 9.0, 9.5, 9.5, 10.0, 11.0, 12.5, and 12.5 for Fe_3O_4, $Fe_{2.95}Gd_{0.05}O_4$, $Fe_{2.9}Gd_{0.1}O_4$, $Fe_{2.85}Gd_{0.15}O_4$, $Fe_{2.8}Gd_{0.2}O_4$, $Fe_{2.75}Gd_{0.25}O_4$, and $Fe_{2.7}Gd_{0.3}O_4$ samples, respectively. Table 1 represents the value of D_{TEM}. An increase of D_{TEM} with an increase of the Gd content for the $Fe_{3-x}Gd_xO_4$ NPs is in good agreement with the crystallite size obtained from XRD studies. All samples have a narrow distribution with $\sigma = 0.1–0.2$.

$$g(D) = \frac{1}{\sqrt{2\pi}\sigma D}\exp\left[-\frac{(\ln D/D_0)^2}{2\sigma^2}\right] \quad (11)$$

where g(D) is the lognormal distribution, $\ln D_0$ is the median, and σ is the standard deviation of $\ln D$.

3.3. EDX analysis

The Energy Dispersive X-ray Spectroscopic (EDX) was used to investigate the weight of the presence elements in the $Fe_{3-x}Gd_xO_4$ NPs. Fig. S2 shows the presence of Fe and O for Fe_3O_4 sample, and the presence of Fe, Gd, and O for $Fe_{3-x}Gd_xO_4$ ($x \neq 0$) samples. Based on data from EDX spectra, the ratio of Fe: Gd: O is calculated and listed in Table 3. Interestingly, the ratio of Fe: Gd were 2.95: 0.06, 2.9: 0.1, 2.85: 0.16, 2.8: 0.19, 2.75: 0.25, and 2.7: 0.29 for $Fe_{2.95}Gd_{0.05}O_4$, $Fe_{2.9}Gd_{0.1}O_4$, $Fe_{2.85}Gd_{0.15}O_4$, $Fe_{2.8}Gd_{0.2}O_4$, $Fe_{2.75}Gd_{0.25}O_4$, and $Fe_{2.7}Gd_{0.3}O_4$ samples, respectively. They are approximately equal to the ratio of Fe: Gd in the chemical formula of $Fe_{3-x}Gd_xO_4$ ($x \neq 0$). These results indicates the existence of Gd^{3+} ions in the Gd-doped Fe_3O_4.

3.4. Raman spectroscopy

Besides XRD analysis, Raman spectroscopy is a crucial tool for examining the structure of materials. Fig. 3 displayed Raman spectrum of the $Fe_{3-x}Gd_xO_4$ NPs, and Fig. 4 presents three peaks of Fe_3O_4 and $Fe_{2.7}Gd_{0.3}O_4$ samples. In accordance with the group theory analysis, the peaks obtained in the spectroscopy can be deconvoluted into individual peaks. For spinel ferrite Fe_3O_4 NPs, their Raman spectra can be predicted five Raman-active bands ($A_{1g} + E_g + 3T_{2g}$) and four infrared-active bands T_{1u} [46]. The Raman modes (A_{1g}, E_g, T_{2g}) were due to the symmetric stretching, symmetric bonding, and asymmetric stretching of O^{2-}, respectively. Raman spectra of Fe_3O_4 displayed five Raman-active phonon modes at 668 cm^{-1} (A_{1g}), 538 cm^{-1} (T_{2g}(1)), 490 cm^{-1} (T_{2g}(2)), 306 cm^{-1} (E_g), and 193 cm^{-1} (T_{2g}(3)) [46].

In practice, there is always the disappearance of one or some of the five Raman-active phonon modes. In other words, some phonon modes weren't observed or reported in previous works. For instance, O. N. Shebanova et al. [46] and L. V. Gasparov et al. [47] didn't found the mode at 490 cm^{-1}. The mode at 193 cm^{-1} wasn't observed in previous works of L. Degiorgi et al. [48] and J. L. Verble et al. [49]. As can be seen in Fig. 5, the Raman spectrum of the $Fe_{3-x}Gd_xO_4$ NPs displays three of five Raman-active phonon modes: A_{1g}, T_{2g}(1), and E_g. Based on these data, three peaks obtained in the spectroscopy of each sample are deconvoluted and presented into individual peaks, which is similar to the three peaks of Fe_3O_4 and $Fe_{2.7}Gd_{0.3}O_4$ samples (Fig. 4). All value of Raman shift at three modes for all samples is listed in Table S1.

Table 3
The EDX estimated elemental composition (% atom) of $Fe_{3-x}Gd_xO_4$ NPs.

Sample	Fe (%)	Gd (%)	O (%)	Ratio Fe: Gd: O
Fe_3O_4	34.19	0	65.81	3: 0: 5.8
$Fe_{2.95}Gd_{0.05}O_4$	30.53	0.72	71.5	2.95: 0.06: 6.9
$Fe_{2.9}Gd_{0.1}O_4$	32.67	1.1	60.3	2.9: 0.1: 5.4
$Fe_{2.85}Gd_{0.15}O_4$	27.21	1.54	75.06	2.85: 0.16: 7.8
$Fe_{2.8}Gd_{0.2}O_4$	33.03	2.03	49.99	2.8: 0.19: 4.2
$Fe_{2.75}Gd_{0.25}O_4$	25.51	2.34	73.17	2.75: 0.25: 7.9
$Fe_{2.7}Gd_{0.3}O_4$	26.55	2.54	67.55	2.7: 0.29: 6.9

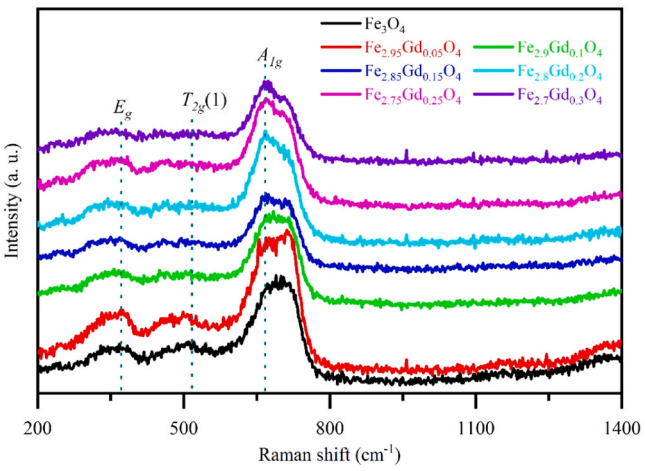

Fig. 3. Raman spectra of $Fe_{3-x}Gd_xO_4$ NPs.

For Fe_3O_4 sample, the A_{1g}, T_{2g}(1), and E_g mode are at 689.4, 509.2, and 349.4 cm^{-1}, respectively. All results of Fe_3O_4 sample is approximately equal to that of Fe_3O_4 of previous works [46]. For $Fe_{3-x}Gd_xO_4$ ($x \neq 0$) samples, the value of Raman shift for three above modes are smaller than that of Fe_3O_4 sample (Table. S1). Figs. 3 and 4 shown that the strong peak is observed at the A_{1g} mode. This A_{1g} mode is responsible for the symmetric stretching of oxygen atoms at the tetrahedral site, and the A_{1g} mode is at 689.4, 687.2, 686.3, 682.7, 679.6, 678.1, and 677.1 cm^{-1} for Fe_3O_4, $Fe_{2.95}Gd_{0.05}O_4$, $Fe_{2.9}Gd_{0.1}O_4$, $Fe_{2.85}Gd_{0.15}O_4$, $Fe_{2.8}Gd_{0.2}O_4$, $Fe_{2.75}Gd_{0.25}O_4$, and $Fe_{2.7}Gd_{0.3}O_4$ samples, respectively. Interestingly, the peak of A_{1g} mode exhibits a left shift with an increase in the content of Gd. This result strongly suggests the replacement of Fe^{3+} ions by Gd^{3+} ions in the $Fe_{3-x}Gd_xO_4$ ($x \neq 0$) samples. This tendency coincides with the results calculated from the XRD analysis.

3.5. Magnetic properties

For Fe_3O_4 NPs, they have the superparamagnetic behavior when their size was smaller than critical diameter, D_{cr}^{SPM}, which was calculated by equation:

$$D_{cr}^{SPM} = \left(\frac{6}{\pi}\frac{25k_BT}{K_{bulk}}\right)^{1/3} \quad (12)$$

where, $K_{bulk} = 9 \times 10^3$ J/m^3, is the bulk value of magnetic anisotropy of Fe_3O_4 [50], k_B is Boltzmann constant, and $T = 300$ K. The obtained D_{cr}^{SPM} value is about of 25 nm, which was larger than all D_{XRD} (8.5 nm) and D_{TEM} (9 nm) values of the Fe_3O_4 sample. Thus, the Fe_3O_4 sample could have the superparamagnetic behavior. In fact, their behavior is found in M-H curve of the Fe_3O_4 sample (Fig. 5(a)). In addition, the $Fe_{3-x}Gd_xO_4$ ($x \neq 0$) samples had no coercivity (Fig. 5(a)), and their size was also smaller than D_{cr}^{SPM} value. Therefore, the superparamagnetic behavior is confirmed for all $Fe_{3-x}Gd_xO_4$ samples. Noting that, this was advantage for them in hyperthermia [2].

However, the replacement of Fe^{3+} ions by Gd^{3+} ions in $Fe_{3-x}Gd_xO_4$ leads to the reduction of saturation magnetization (M_S). Fig. 5(a) and Table. S2 found that the M_S value decreased from 66.7 emu/g (Fe_3O_4 sample) to 46.1 emu/g ($Fe_{2.7}Gd_{0.3}O_4$ sample). This replacement is also predicted to be the reason for the reduction of magnetic anisotropy (K)

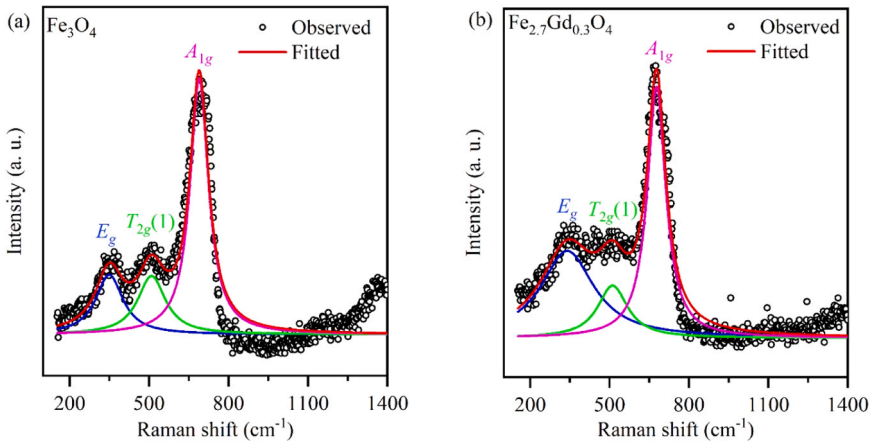

Fig. 4. Lorentzian multiple peak fitted Raman spectra of (a) Fe_3O_4 and (b) $Fe_{2.7}Gd_{0.3}O_4$ samples.

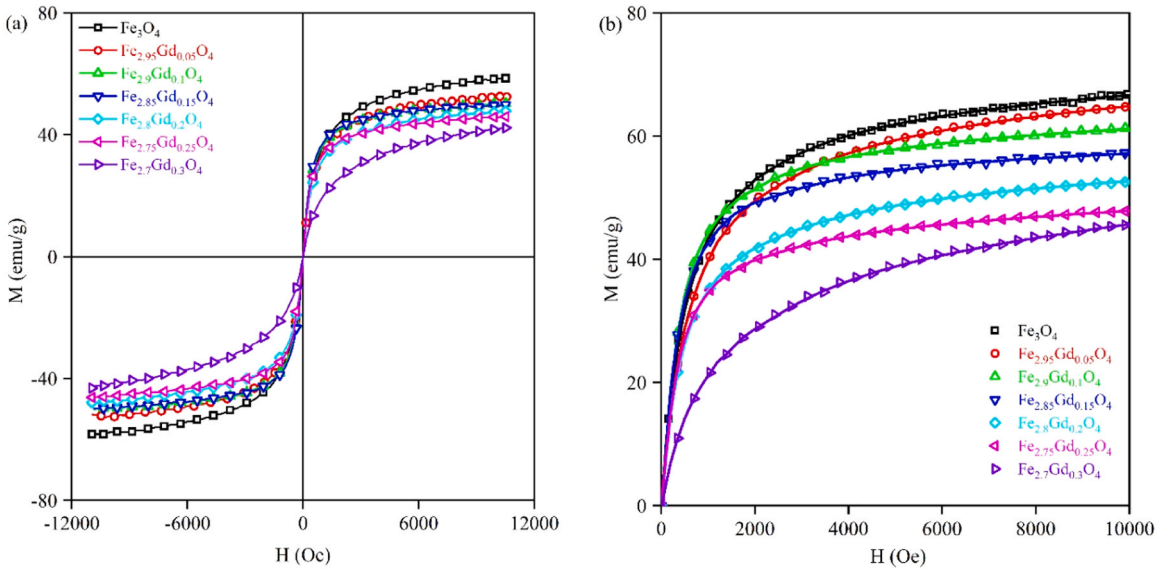

Fig. 5. (a) M-H curves of $Fe_{3-x}Gd_xO_4$ NPs and (b) The initial magnetization curves with the fitting curve (solid line) assuming "the law of approach to saturation" for all samples.

of $Fe_{3-x}Gd_xO_4$ NPs. In order to confirm this prediction, the value of K for each sample is determined by fitting the initial data of M-H curves under the "law of approach to saturation" [51]:

$$M(H) = M_s\left(1 - \frac{k_BT}{M_sVH} - \frac{4K^2}{15M_S^2H^2} - \ldots\right) + \chi_pH \quad (13)$$

in which, χ_p is the high-field susceptibility, k_B is Boltzmann constant, V is volume of nanoparticle, M_S is saturation magnetization, K is magnetic anisotropy, H is the field amplitude, and T is temperature. Fig. 5(b) depicts the good fit of the initial magnetization curves using Eq. (13) for Fe_3O_4, $Fe_{2.95}Gd_{0.05}O_4$, $Fe_{2.9}Gd_{0.1}O_4$, $Fe_{2.85}Gd_{0.15}O_4$, $Fe_{2.8}Gd_{0.2}O_4$, $Fe_{2.75}Gd_{0.25}O_4$, and $Fe_{2.7}Gd_{0.3}O_4$ samples. The values of K are also shown in Table. S2.

As can be seen in Fig. 5 and Table. S2, the K value for the $Fe_{3-x}Gd_xO_4$ NPs has the same trend as compared to that of M_S value. For Fe_3O_4 sample, the M_S value is smaller than that of bulk Fe_3O_4 (90 emu/g) [40]. This extension could be explained by a core–shell model with the presence of a disordered layer, or dead layer in the shells of nanoparticles [52]. In addition, the M_S value decreased from 66.7 emu/g (Fe_3O_4 sample) to 46.1 emu/g ($Fe_{2.7}Gd_{0.3}O_4$ sample), which is in consistent with the above prediction. These interesting results are explained by two reasons. Firstly, the magnetic property of a magnetic material is the sum of the magnetic moments per unit volume of that material. When the concentration of Gd^{3+} ions increases, the number of Fe^{3+} ions decreases. In addition, I. Alotaibi et al. indicated that the decrease of the M_S value with increasing Gd^{3+} ions concentration might be attributed to the insertion of large Gd^{3+} ions in the octahedral sites in Gd-doped γ-Fe_2O_3, which will affect Fe–Gd interactions and induce a decrease in long-range magnetic ordering [16]. Similarly, this replacement led also to the disruption in the long-range order of magnetic spins in pure Fe_3O_4 NPs [53]. Thus, when replacing Fe^{3+} ions by Gd^{3+} ions in Fe_3O_4 NPs, the magnetism of the whole system will decrease. This tendency of M_S was also found in previous works. For instance, N. D. Thorat et al. found the reduction of M_S value when the content of Gd^{3+} ions increased [24]. As a general trend, the reduction of M_S for doped samples was also observed in the previous works about Gd-doped Fe_3O_4 NPs [31], or Gd-doped other NPs [42,44]. Besides, one should notice that the magnetic properties strongly depend on the crystal size, which related to the competition between the two effects: surface effect and the finite size effect. This is the second reason for these tendencies.

As can be seen in Table. S2, all K values are larger than the bulk value of magnetic anisotropy of Fe_3O_4 (9 kJ/m^3 [50]). As the size decreased, the surface effect raised, resulting in a increase in the K value. For

example, G. F. Goya found that the value of K was ~ 70 kJ/m^3 for Fe_3O_4 (10 nm) NPs [54]. Similarly, the value of K of Fe_3O_4 sample was 69.2 kJ/m^3, which was ~ 7.7 times higher than that of the bulk value. For the $Fe_{3-x}Gd_xO_4$ ($x \neq 0$) samples in this work, the Gd^{3+} ions acted inhibitors of FO's nanoparticle formation during the reaction to create these samples, the value of size (D_{XRD} and D_{TEM}) increased with an increase in x content. Therefore, the value of K decreases from 52.3 kJ/m^3 ($Fe_{2.95}Gd_{0.05}O_4$) to 31.5 kJ/m^3 ($Fe_{2.7}Gd_{0.3}O_4$). This result is completely consistent with the experimental results on these decrease from nanoparticle with size [51]. In previous works in hyperthermia, magnetic anisotropy was considered as an important parameter in order to enhance the effectiveness of samples [55]. Especially, these above results indicates that these samples ($Fe_{3-x}Gd_xO_4$ with $0.05 \leq x \leq 0.3$) with a large change magnetic anisotropy (31.5 – 52.3 kJ/m^3) in small size (7.6 – 8.9 nm of D_{XRD}, 9.0 – 12.5 nm of D_{TEM}) were suitable for biomedical applications [55,56]. Thus, doping Fe_3O_4 NPs by Gd^{3+} ions was a useful approach in order to adjust magnetic properties properly to the requirement of biomedical applications.

3.6. Hyperthermia testing

In practical hyperthermia applications, NPs should have a diameter in the range of 10–50 nm, the saturation magnetization is large enough and satisfies the following conditions: stability in magnetic nanofluids; and the body human must only receive a little number of NPs, but the heat produced by the MIH effect must be sufficient [2]. In this work, the $Fe_{3-x}Gd_xO_4$ ($0 \leq x \leq 0.3$) NPs with medium saturation magnetization (46.1 – 66.7 emu/g) in small size (7.6 – 8.9 nm of D_{XRD}, 9.0 – 12.5 nm of D_{TEM}) could be suitable for hyperthermia applications. Thus, the magnetic induction heating rates of the $Fe_{3-x}Gd_xO_4$ NPs were measured, which was presented in Fig. 6. The *SAR* values of all samples were computed by Eqs. (1) and (2), and listed in Table 4.

In order to compare the heating efficiency of NPs from various works, *ESAR* (Effective Specific Absorption Rate) acts as an independent parameter, which normalizes the value of *SAR* with respect to an ac field (H, f) by the following equation:

$$ESAR = \frac{SAR}{H^2 f} \tag{14}$$

with concentration of 5 mg/mL at the frequency (f) of 450 kHz and amplitude (H) of 200 Oe.

As can be seen in Table 4, the *SAR* value are 23.4, 44.3, 62.7, 147.1,

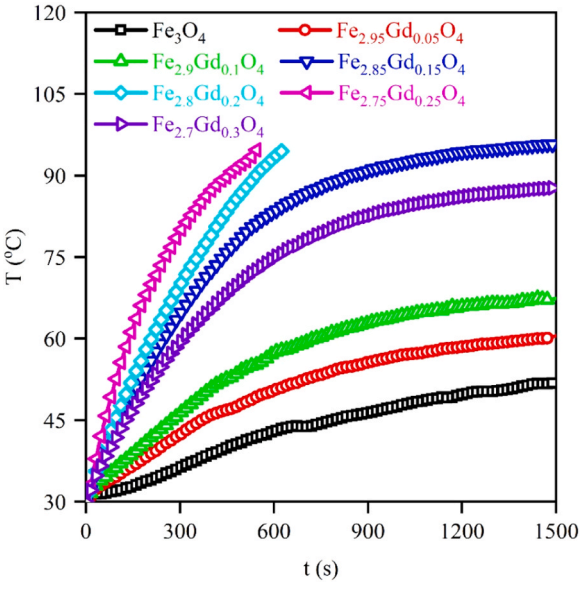

Fig. 6. Magnetic heating curves T(t) of $Fe_{3-x}Gd_xO_4$ NPs.

Table 4
The values of *SAR*, *ESAR*, and SAR/M_S for $Fe_{3-x}Gd_xO_4$ NPs with concentration of 5 mg/mL at $H = 200$ Oe, $f = 450$ kHz.

Sample	*SAR* (W/g)	*ESAR* (nHm^2/kg)	$\frac{SAR}{M_S}$ (W/emu)
Fe_3O_4	23.4	0.21	0.4
$Fe_{2.95}Gd_{0.05}O_4$	44.3	0.39	0.7
$Fe_{2.9}Gd_{0.1}O_4$	62.7	0.55	1
$Fe_{2.85}Gd_{0.15}O_4$	147.1	1.29	2.6
$Fe_{2.8}Gd_{0.2}O_4$	168.0	1.47	3.2
$Fe_{2.75}Gd_{0.25}O_4$	237.4	2.08	4.9
$Fe_{2.7}Gd_{0.3}O_4$	114.5	1.00	2.5

168.0, 237.04, and 114.5 W/g for Fe_3O_4, $Fe_{2.95}Gd_{0.05}O_4$, $Fe_{2.9}Gd_{0.1}O_4$, $Fe_{2.85}Gd_{0.15}O_4$, $Fe_{2.8}Gd_{0.2}O_4$, $Fe_{2.75}Gd_{0.25}O_4$, and $Fe_{2.7}Gd_{0.3}O_4$ samples, respectively. The value of *ESAR* are 0.21, 0.39, 0.55, 1.29, 1.47, 2.08, and 1 nHm^2/kg for the respective samples. The *ESAR* value of $Fe_{2.75}Gd_{0.25}O_4$ is larger than that of 2–5 % Gd doped Fe_3O_4 NPs [31]. These results indicate that the $Fe_{2.75}Gd_{0.25}O_4$ sample could be suitable for hyperthermia applications. Interestingly, all values of *SAR* for the $Fe_{3-x}Gd_xO_4$ ($x \neq 0$) samples are larger than that of Fe_3O_4 sample (23.4 W/g) and all reach magnetic hyperthermia temperature (42 °C) in short time. For example, the $Fe_{2.75}Gd_{0.25}O_4$ sample could reach magnetic hyperthermia temperature in ~ one minute. This tendency was found in the previous works about Gd-doped spinel ferrites NPs [18,31]. Especially, there was the existence of the peak of *SAR* versus the Gd content (x) in the $Fe_{3-x}Gd_xO_4$ ($x \neq 0$) samples, which was observed in previous work of D. Jaison et al. [18] and this work. Noting that the proportional relationship between M_S and *SAR* was found in previous works [33], thus, the increase of *SAR* with the reduction of M_S for doped samples and the existence of peak of the plot *SAR* versus Gd^{3+} ions concentration were interesting unusual results.

In order to explain these interesting results, the theoretical *SAR* (SAR_{theo}) value was calculated. In general, the heat generation mechanism of the rapid heating process in the early stages is due to the contribution of hysteresis loss, recovery loss (N é el, Brown) and eddy current loss. For superparamagnetic NPs, the total loss power density is mainly due to loss mechanisms related to relaxation losses, and the value of *SAR* is calculated based on Linear Theory Response (LRT). As above mentioned, because all samples had superparamagnetic behavior, the theoretical *SAR* value was computed in the framework of LRT (details in Ref. [33]). Up to date, several works claimed that the SAR value depend strongly on nanoparticle size, saturation magnetization, magnetic anisotropy, inter-nanoparticle interaction as well as AMF [33,34,57,58]. Especially, several parameters including size, saturation magnetization, and magnetic anisotropy were evaluated as important parameters in the enhancement of *SAR* value [33,40,56]. Interestingly, doping made a change simultaneously in nanoparticle size, saturation magnetization, and magnetic anisotropy as compared to pure Fe_3O_4 NPs in our work; thus, the explanation for the enhancement of the *SAR* value of the doped sample help insight into the role of these above parameters.

Firstly, the doped sample $Fe_{3-x}Gd_xO_4$ ($x \neq 0$) NPs could be seen as Fe_3O_4 NPs with different values of D, M_S, and K. As can be seen in Table 1, the D_{TEM} for all samples are in the range of 9 – 13. In addition, the value of K changes with a large range from 31.5 kJ/m^3 to 69.2 kJ/m^3. Therefore, the SAR_{theo} is computed as a function of K value with various D (9, 10, 11, 12, and 13 nm) in order to compare with experimental results. The obtained plot of SAR_{theo} versus K for Fe_3O_4 NPs with various nanoparticle sizes is presented in Fig. 7. Second, there was a conflict between the proportional relationship of M_S and *SAR* [33] with the enhancement of *SAR* in the M_S reduction (Tables S2 and 4) for doped samples. This indicated that the increase in *SAR* didn't relate to M_S. Therefore, the enhancement of *SAR* might relate to nanoparticle size and magnetic anisotropy.

In order to compare the experimental tendency with theoretical results, the ratio $\frac{SAR}{M_S}$, which normalizes the value of *SAR* with respect to M_S

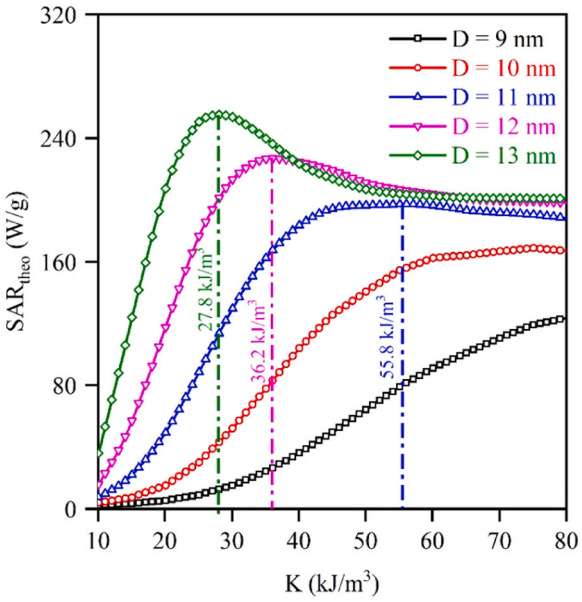

Fig. 7. Dependence of SAR_{theo} on K value with various diameters.

value, was also shown in Table. S2. The obtained results find that the ratio reach maximum value for $Fe_{2.75}Gd_{0.25}O_4$ sample. Fig. 7 finds the existence of the peaks for SAR_{theo} (K) at 27.8 kJ/m^3, 36.2 kJ/m^3, and 55.8 kJ/m^3 for D of 13 nm, 12 nm, and 11 nm, respectively. Interestingly, these points of SAR_{theo} values for all samples have the same order as compared with experimental results. For instance, the SAR value at 69.2 kJ/m3 on the black line (SAR versus K for $D = 9$ nm) is smaller than the SAR value at 52.3 kJ/m3 on the red line (SAR versus K for $D =$ 10 nm). The SAR value reaches maximum value at 36.2 kJ/m^3 on the plot of SAR_{theo} (K) for $D = 13$ nm, which is equal to the K value of $Fe_{2.75}Gd_{0.25}O_4$ sample ($D_{TEM} = 12.5 \pm 0.5$). Although both of $Fe_{2.75}Gd_{0.25}O_4$ and $Fe_{2.7}Gd_{0.3}O_4$ samples have same size of D_{TEM}, the SAR value of $Fe_{2.75}Gd_{0.25}O_4$ sample is larger than that of $Fe_{2.7}Gd_{0.3}O_4$ sample because of the effect of magnetic anisotropy (as can be seen in Fig. 7). This role of K was also observed in previous works [40,55,56, 59]. The good agreement between experimental and theoretical results indicated that the important role of K and D in optimizing SAR value for $Fe_{3-x}Gd_xO_4$ NPs.

Next, the hyperthermia test for the $Fe_{2.75}Gd_{0.25}O_4$ sample is conducted in ac fields with an amplitude of 200 Oe with various concentrations, or an amplitude between 100 and 300 Oe at 1 mg/mL (Fig. S4). All experiments were fixed at the frequency of 450 kHz. The value of SAR, and $ESAR$ were listed in Table S3. As can be seen in Table. S3, the value of SAR for $Fe_{2.75}Gd_{0.25}O_4$ NPs are 204.8, 150.5, 115.6, 128.4, and 237.4 W/g for the concentration of 1, 2, 3, 4, and 5 mg/mL, respectively. The reduction of SAR occurred when the concentration changed from 1 mg/mL to 3 mg/mL. In contrast, an increase of SAR value with an increase of the concentration is found in the range of 3 – 5 mg/mL. This phenomenon was also found in the work of J.-w. Kim et al. [60], which is caused by the effect of inter-particle distance. L. T. Dat et al. claimed that the relationship between K value and concentration (or inter-particle distance) led to the dependence of SAR on concentration [40]. Besides, the high value of SAR (204.8 W/g) and $ESAR$ (1.80 nHm^2/kg) of $Fe_{2.75}Gd_{0.25}O_4$ sample at small concentration (1 mg/mL) indicates that this sample could be seen as a heating mediator as low concentration. This was advantage of this sample for hyperthermia applications. Interestingly, although the SAR value of $Fe_{2.75}Gd_{0.25}O_4$ sample increases from 87.8 W/g to 380.4 W/g with an increase of H value, the $ESAR$ value reaches the maximum value (3.08 nHm^2/kg) at 100 Oe of amplitude. All results of $Fe_{2.75}Gd_{0.25}O_4$ sample indicates that this sample could be acted as an efficiency heating mediator at the low concentration, and at the low amplitude of ac fields.

4. Conclusion

In summary, the Gd^{3+} ions have a significant impact on the structural, optical, and magnetic properties of Fe_3O_4 NPs. For the doped samples ($Fe_{3-x}Gd_xO_4$ NPs, $x \neq 0$), the structural parameters including lattice parameter (a), crystallite size (D_{XRD}), X-ray density (ρ_{XRD}), and D_{TEM} increased with an increase of the number of Gd^{3+} ions. The replacement of Fe^{3+} ions by Gd^{3+} ions causing an increase of E_g value and the reduction of M_S and K values was demonstrated. Interestingly, although the existence of a reduction in the M_S value for $Fe_{3-x}Gd_xO_4$ NPs, the experimental results indicated that all doped samples can be used as an efficiency heating mediator in hyperthermia applications. Furthermore, the maximal SAR value was of 237.4 W/g at $x = 0.25$ ($Fe_{2.75}Gd_{0.25}O_4$ sample), that proved to the dependence of SAR on magnetic anisotropy and nanoparticle size. These findings suggest that doping was an effective strategy for optimizing as-synthesized NPs to enable heating efficiency in hyperthermia applications.

CRediT authorship contribution statement

Luu Huu Nguyen: Writing – review & editing, Conceptualization, Writing – original draft preparation, Writing – review & editing. **Nguyen Hoai Nam:** Investigation, Formal analysis. **Le The Tam:** Investigation, Formal analysis. **Dinh Van Tuan:** Methodology, Data curation. **Nguyen Xuan Truong:** Methodology, Data curation. **Nguyen Van Quynh:** Methodology, Formal analysis. **Phan Thi Hong Tuyet:** Methodology, Formal analysis. **Ha Phuong Thu:** Data curation. **Do Hung Manh:** Data curation. **Pham Hong Nam:** Conceptualization, Writing – review & editing, Supervision. **Pham Thanh Phong**: Review & Editing.

Declaration of Competing Interest

The authors declare that they have no known competing financial interests or personal relationships that could have appeared to influence the work reported in this paper.

Data Availability

Data will be made available on request.

Acknowledgments

This work was supported by Vietnam Academy of Science and Technology (VAST) under grant number VAST03.01/23-24. L. H. Nguyen is thankful to Van Lang University.

Appendix A. Supporting information

Supplementary data associated with this article can be found in the online version at doi:10.1016/j.jallcom.2023.172205.

References

[1] M. Mahmoodi, B. Aslibeiki, M. Abdolalipour Sakha, M. Zarei, Oleaster seed-derived activated carbon/ferrite nanocomposite for Pb^{2+} removal from wastewater, Mater. Chem. Phys. 300 (2023), 127536, https://doi.org/10.1016/j.matchemphys.2023.127536.
[2] K.K. Kefeni, T.A.M. Msagati, T.T. Nkambule, B.B. Mamba, Spinel ferrite nanoparticles and nanocomposites for biomedical applications and their toxicity, Mater. Sci. Eng. C. 107 (2020), https://doi.org/10.1016/j.msec.2019.110314, 110314(19).
[3] C.R. Kalaiselvan, S.S. Laha, S.B. Somvanshi, T.A. Tabish, N.D. Thorat, N.K. Sahu, Manganese ferrite ($MnFe_2O_4$) nanostructures for cancer theranostics, Coord. Chem. Rev. 473 (2022), 214809, https://doi.org/10.1016/j.ccr.2022.214809.
[4] S.B. Somvanshi, P.B. Kharat, T.S. Saraf, S.B. Somwanshi, S.B. Shejul, K.M. Jadhav, Multifunctional nano-magnetic particles assisted viral RNA-extraction protocol for

potential detection of COVID-19, Mater. Res. Innov. 25 (2021) 169–174, https://doi.org/10.1080/14328917.2020.1769350.
[5] O.M. Lemine, N. Madkhali, M. Hjiri, N.A. All, M.S. Aida, Comparative heating efficiency of hematite (α-Fe_2O_3) and nickel ferrite nanoparticles for magnetic hyperthermia application, Ceram. Int. 46 (2020) 28821–28827, https://doi.org/10.1016/j.ceramint.2020.08.047.
[6] S.B. Somvanshi, P.B. Kharat, K.M. Jadhav, Surface functionalized superparamagnetic Zn-Mg ferrite nanoparticles for magnetic hyperthermia application towards noninvasive cancer treatment, Macromol. Symp. 400 (2021), 2100124, https://doi.org/10.1002/masy.202100124.
[7] P.B. Kharat, S.B. Somvanshi, S.B. Somwanshi, A.M. Mopari, Synthesis, characterization and hyperthermic evaluation of PEGylated Superparamagnetic $MnFe_2O_4$ ferrite nanoparticles for cancer therapeutics applications, Macromol. Symp. 400 (2021), 2100130, https://doi.org/10.1002/masy.202100130.
[8] O.M. Lemine, N. Madkhali, M. Alshammari, S. Algessair, A. Gismelseed, L. El Mir, M. Hjiri, A.A. Yousif, K. El-Boubbou, Maghemite (γ-Fe_2O_3) and γ-Fe_2O_3-TiO_2 nanoparticles for magnetic hyperthermia applications: synthesis, characterization and heating efficiency, Materials 14 (2021) 5691, https://doi.org/10.3390/ma14195691.
[9] P.B. Kharat, S.B. Somvanshi, P.P. Khirade, K.M. Jadhav, Induction heating analysis of surface-functionalized nanoscale $CoFe_2O_4$ for magnetic fluid hyperthermia toward noninvasive cancer treatment, ACS Omega 5 (2020) 23378–23384, https://doi.org/10.1021/acsomega.0c03332.
[10] S.R. Patade, D.D. Andhare, S.B. Somvanshi, S.A. Jadhav, M.V. Khedkar, K. M. Jadhav, Self-heating evaluation of superparamagnetic $MnFe_2O_4$ nanoparticles for magnetic fluid hyperthermia application towards cancer treatment, Ceram. Int. 46 (2020) 25576–25583, https://doi.org/10.1016/j.ceramint.2020.07.029.
[11] S.B. Somvanshi, N.D. Thorat, Nanoplatforms for cancer imagining, in: N.D. Thorat (Ed.), Advances in Image-Guided Cancer Nanomedicine, IOP Publishing, Bristol, UK, 2022, 3-1-3-62.
[12] S.B. Somvanshi, N.D. Thorat, Synergy between nanomedicine and tumor imaging, in: N.D. Thorat (Ed.), Advances in Image-Guided Cancer Nanomedicine, IOP Publishing, Bristol, UK, 2022, 4-1-4-61.
[13] S.B. Somvanshi, P.B. Kharat, M.V. Khedkar, K.M. Jadhav, Hydrophobic to hydrophilic surface transformation of nano-scale zinc ferrite via oleic acid coating: Magnetic hyperthermia study towards biomedical applications, Ceram. Int. 46 (2020) 7642–7653, https://doi.org/10.1016/j.ceramint.2019.11.265.
[14] S.B. Somvanshi, S.R. Patade, D.D. Andhare, S.A. Jadhav, M.V. Khedkar, P. B. Kharat, P.P. Khirade, K.M. Jadhav, Hyperthermic evaluation of oleic acid coated nano-spinel magnesium ferrite: Enhancement via hydrophobic-to-hydrophilic surface transformation, J. Alloy. Compd. 835 (2020), https://doi.org/10.1016/j.jallcom.2020.155422, 155422.
[15] S.B. Somvanshi, S.A. Jadhav, S.S. Gawali, K. Zakde, K.M. Jadhav, Core-shell structured superparamagnetic Zn-Mg ferrite nanoparticles for magnetic hyperthermia applications, J. Alloy. Compd. 947 (2023), 169574, https://doi.org/10.1016/j.jallcom.2023.169574.
[16] I. Alotaibi, M.S. Alshammari, S. Algessair, N. Madkhali, N.A. All, M. Hjiri, S. A. Alrub, L. El Mir, O.M. Lemine, Synthesis, characterization and heating efficiency of Gd-doped maghemite (γ-Fe_2O_3) nanoparticles for hyperthermia application, Phys. B Condens. Matter 625 (2022), 413510, https://doi.org/10.1016/j.physb.2021.413510.
[17] S.A. Jadhav, S.B. Somvanshi, S.S. Gawali, K. Zakade, K.M. Jadhav, Rare earth-doped mixed Ni–Cu–Zn ferrites as an effective photocatalytic agent for active degradation of Rhodamine B dye, J. Rare Earths (2023), https://doi.org/10.1016/j.jre.2023.03.004.
[18] D. Jaison, A. Gangwar, P.N. Kishore, G. Chandrasekaran, M. Mothilal, Effect of Gd^{3+} substitution on proton relaxation and magnetic hyperthermia efficiency of cobalt ferrite nanoparticles, Mater. Res. Express 7 (2020), 064009, https://doi.org/10.1088/2053-1591/ab9378.
[19] H. Jalili, B. Aslibeiki, A. Hajalilou, O. Musalu, L.P. Ferreira, M.M. Cruz, Bimagnetic hard/soft and soft/hard ferrite nanocomposites: Structural, magnetic and hyperthermia properties, Ceram. Int. 48 (2022) 4886–4896, https://doi.org/10.1016/j.ceramint.2021.11.025.
[20] H. Jalili, B. Aslibeiki, A. Ghotbi Varzaneh, V.A. Chernenko, The effect of magneto-crystalline anisotropy on the properties of hard and soft magnetic ferrite nanoparticles, Beilstein J. Nanotechnol. 10 (2019) 1348–1359, https://doi.org/10.3762/bjnano.10.133.
[21] V.A. Bharati, S.B. Somvanshi, A.V. Humbe, V.D. Murumkar, V.V. Sondur, K. M. Jadhav, Influence of trivalent Al–Cr co-substitution on the structural, morphological and Mössbauer properties of nickel ferrite nanoparticles, J. Alloy. Compd. 821 (2020), 153501, https://doi.org/10.1016/j.jallcom.2019.153501.
[22] A.V. Humbe, J.S. Kounsalye, S.B. Somvanshi, A. Kumar, K.M. Jadhav, Cation distribution, magnetic and hyperfine interaction studies of Ni–Zn spinel ferrites: role of Jahn Teller ion (Cu^{2+}) substitution, Mater. Adv. 1 (2020) 880–890, https://doi.org/10.1039/D0MA00251H.
[23] F. Javed, M.A. Abbas, M.I. Asad, N. Ahmed, N. Naseer, H. Saleem, A. Errachid, N. Lebaz, A. Elaissari, N.M. Ahmad, Gd^{3+} Doped $CoFe_2O_4$ nanoparticles for targeted drug delivery and magnetic resonance imaging, Magnetochemistry 7 (16) (2021) 47, https://doi.org/10.3390/magnetochemistry7040047.
[24] N.D. Thorat, R.A. Bohara, H.M. Yadav, S.A.M. Tofail, Multi-modal MR imaging and magnetic hyperthermia study of Gd doped Fe_3O_4 nanoparticles for integrative cancer therapy, RSC Adv. 6 (2016) 94967–94975, https://doi.org/10.1039/C6RA20135K.
[25] S. Zheng, S. Jin, M. Jiao, W. Wang, X. Zhou, J. Xu, Y. Wang, P. Dou, Z. Jin, C. Wu, Tumor-targeted Gd-doped mesoporous Fe_3O_4 nanoparticles for T_1/T_2 MR imaging guided synergistic cancer therapy, Drug Deliv. 28 (2021) 787–799, https://doi.org/10.1080/10717544.2021.1909177.
[26] J. Giri, P. Pradhan, T. Sriharsha, D. Bahadur, Preparation and investigation of potentiality of different soft ferrites for hyperthermia applications, J. Appl. Phys. 97 (2005), 10Q916, https://doi.org/10.1063/1.1855131.
[27] E. Fantechi, C. Innocenti, M. Albino, E. Lottini, C. Sangregorio, Influence of cobalt doping on the hyperthermic efficiency of magnetite nanoparticles, J. Magn. Magn. Mater. 380 (2015) 365–371, https://doi.org/10.1016/j.jmmm.2014.10.082.
[28] J.S. Anandhi, T. Arun, R.J. Joseyphus, Role of magnetic anisotropy on the heating mechanism of Co-doped Fe_3O_4 nanoparticles, Phys. B Condens. Matter 598 (2020), https://doi.org/10.1016/j.physb.2020.412429, 412429-412437.
[29] J.S. Anandhi, G.A. Jacob, R.J. Joseyphus, Factors affecting the heating efficiency of Mn-doped Fe_3O_4 nanoparticles, J. Magn. Magn. Mater. 512 (2020), 166992, https://doi.org/10.1016/j.jmmm.2020.166992.
[30] X. Koutsoumbou, I. Tsiaoussis, G.A. Bulai, O.F. Caltun, O. Kalogirou, C. Sarafidis, $CoFe_{2-x}RE_xO_4$ (RE= Dy, Yb, Gd) magnetic nanoparticles for biomedical applications, Phys. B Condens. Matter 606 (2021), https://doi.org/10.1016/j.physb.2021.412849, 412849(11).
[31] K.P. Hazarika, R. Fopase, L. Pandey, J.P. Borah, Influence of Gd-doping on structural, magnetic, and self-heating properties of Fe_3O_4 nanoparticles towards magnetic hyperthermia applications, Phys. B Condens. Matter 3 (2022), https://doi.org/10.1016/j.physb.2022.414237, 414237(13).
[32] B. Aslibeiki, M.H. Ehsani, F. Nasirzadeh, M.A. Mohammadi, The effect of interparticle interactions on spin glass and hyperthermia properties of Fe_3O_4 nanoparticles, Mater. Res. Express 4 (2017), 075051, https://doi.org/10.1088/2053-1591/aa7eb1.
[33] P.T. Phong, L.H. Nguyen, I.-J. Lee, N.X. Phuc, Computer simulations of contributions of Néel and Brown relaxation to specific loss power of magnetic fluids in hyperthermia, J. Electron. Mater. 46 (2017) 2393–2405, https://doi.org/10.1007/s11664-017-5302-6.
[34] R.E. Rosensweig, Heating magnetic fluid with alternating magnetic field, J. Magn. Magn. Mater. 252 (2002) 370–374, https://doi.org/10.1016/S0304-8853(02)00706-0.
[35] J. Tauc, R. Grigorovici, A. Vancu, Optical properties and electronic structure of amorphous germanium, Phys. Status Solidi B 15 (1966) 627–637, https://doi.org/10.1002/pssb.19660150224.
[36] A. Radoń, A. Drygała, Ł. Hawełek, D. Łukowiec, Structure and optical properties of Fe_3O_4 nanoparticles synthesized by co-precipitation method with different organic modifiers, Mater. Charact. 131 (2017) 148–156, https://doi.org/10.1016/j.matchar.2017.06.034.
[37] Y. Zhao, M.E. Sadat, A. Dunn, H. Xu, C.-H. Chen, W. Nakasuga, R.C. Ewing, D. Shi, Photothermal effect on Fe_3O_4 nanoparticles irradiated by white-light for energy-efficient window applications, Sol. Energy Mater. Sol. Cells 161 (2017) 247–254, https://doi.org/10.1016/j.solmat.2016.11.039.
[38] M.E. Sadat, M.K. Baghbador, A.W. Dunn, H.P. Wagner, R.C. Ewing, J. Zhang, H. Xu, G.M. Pauletti, D.B. Mast, D. Shi, Photoluminescence and photothermal effect of Fe_3O_4 nanoparticles for medical imaging and therapy, Appl. Phys. Lett. 105 (2014), 091903, https://doi.org/10.1063/1.4895133.
[39] A. Manikandan, J.J. Vijaya, J.A. Mary, L.J. Kennedy, A. Dinesh, Structural, optical and magnetic properties of Fe_3O_4 nanoparticles prepared by a facile microwave combustion method, J. Ind. Eng. Chem. 20 (2014) 2077–2085, https://doi.org/10.1016/j.jiec.2013.09.035.
[40] L.T. Dat, L.H. Nguyen, N.H. Nam, T.D. Van, N.X. Truong, V.-Q. Nguyen, P. T. Phong, P.H. Nam, Dependence of specific absorption rate on concentration of Fe_3O_4 nanoparticles: from the prediction of Monte Carlo simulations to experimental results, J. Nanopart. Res. 24 (2022) 1–13, https://doi.org/10.1007/s11051-022-05596-z.
[41] B. Aslibeiki, P. Kameli, H. Salamati, The role of Ag on dynamics of superspins in $MnFe_{2-x}Ag_xO_4$ nanoparticles, J. Nanopart. Res. 15 (2013), 1430, https://doi.org/10.1007/s11051-013-1430-y.
[42] M. Yousaf, S. Nazir, M. Akbar, M.N. Akhtar, A. Noor, E. Hu, M.A.K.Y. Shah, Y. Lu, Structural, magnetic, and electrical evaluations of rare earth Gd^{3+} doped in mixed Co–Mn spinel ferrite nanoparticles, Ceram. Int. 48 (2022) 578–586, https://doi.org/10.1016/j.ceramint.2021.09.136.
[43] S.B. Somvanshi, S.A. Jadhav, M.V. Khedkar, P.B. Kharat, S.D. More, K.M. Jadhav, Structural, thermal, spectral, optical and surface analysis of rare earth metal ion (Gd^{3+}) doped mixed Zn–Mg nano-spinel ferrites, Ceram. Int. 46 (2020) 13170–13179, https://doi.org/10.1016/j.ceramint.2020.02.091.
[44] R.S. Yadav, I. Kuritka, J. Vilcakova, J. Havlica, L. Kalina, P. Urbánek, M. Machovsky, D. Skoda, M. Masař, M. Holek, Sonochemical synthesis of Gd^{3+} doped $CoFe_2O_4$ spinel ferrite nanoparticles and its physical properties, Ultrason. Sonochem. 40 (2018) 773–783, https://doi.org/10.1016/j.ultsonch.2017.08.024.
[45] A.B. Bhosale, S.B. Somvanshi, V.D. Murumkar, K.M. Jadhav, Influential incorporation of RE metal ion (Dy^{3+}) in yttrium iron garnet (YIG) nanoparticles: Magnetic, electrical and dielectric behaviour, Ceram. Int. 46 (2020) 15372–15378, https://doi.org/10.1016/j.ceramint.2020.03.081.
[46] O.N. Shebanova, P. Lazor, Raman spectroscopic study of magnetite ($FeFe_2O_4$): a new assignment for the vibrational spectrum, J. Solid State Chem. 174 (2003) 424–430, https://doi.org/10.1016/S0022-4596(03)00294-9.
[47] L.V. Gasparov, D.B. Tanner, D.B. Romero, H. Berger, G. Margaritondo, L. Forró, Infrared and Raman studies of the Verwey transition in magnetite, Phys. Rev. B 62 (2000) 7939–7944, https://doi.org/10.1103/PhysRevB.62.7939.
[48] L. Degiorgi, I. Blatter-Mörke, P. Wachter, Magnetite: phonon modes and the Verwey transition, Phys. Rev. B 35 (1987) 5421–5424, https://doi.org/10.1103/PhysRevB.35.5421.

[49] J.L. Verble, Temperature-dependent light-scattering studies of the Verwey transition and electronic disorder in magnetite, Phys. Rev. B 9 (1974) 5236–5248, https://doi.org/10.1103/PhysRevB.9.5236.
[50] L.H. Nguyen, V.T.K. Oanh, P.H. Nam, D.H. Doan, N.X. Truong, N.X. Ca, P.T. Phong, L.V. Hong, T.D. Lam, Increase of magnetic hyperthermia efficiency due to optimal size of particles: theoretical and experimental results, J. Nanopart. Res. 22 (2020), 258, https://doi.org/10.1007/s11051-020-04986-5.
[51] L.H. Nguyen, N.X. Phuc, D.H. Manh, N.H. Nam, N.X. Truong, N.V. Quynh, P. T. Phong, P.H. Nam, Size-Dependent Magnetic Heating of $MnFe_2O_4$ Nanoparticles, J. Electron. Mater. 50 (2021) 5318–5326, https://doi.org/10.1007/s11664-021-09056-7.
[52] B. Aslibeiki, P. Kameli, H. Salamati, The effect of dipole-dipole interactions on coercivity, anisotropy constant, and blocking temperature of $MnFe_2O_4$ nanoparticles, J. Appl. Phys. 119 (2016), 063901, https://doi.org/10.1063/1.4941388.
[53] N. Xiao, W. Gu, H. Wang, Y. Deng, X. Shi, L. Ye, T_1–T_2 dual-modal MRI of brain gliomas using PEGylated Gd-doped iron oxide nanoparticles, J. Colloid Interface Sci. 417 (2014) 159–165, https://doi.org/10.1016/j.jcis.2013.11.020.
[54] G.F. Goya, T.S. Berquo, F.C. Fonseca, M.P. Morales, Static and dynamic magnetic properties of spherical magnetite nanoparticles, J. Appl. Phys. 94 (2003) 3520–3528, https://doi.org/10.1063/1.1599959.
[55] L.H. Nguyen, P.T. Phong, P.H. Nam, D.H. Manh, N.T.K. Thanh, L.D. Tung, N. X. Phuc, The role of anisotropy in distinguishing domination of Néel or Brownian relaxation contribution to magnetic inductive heating: orientations for biomedical applications, Materials 14 (2021) 1875, https://doi.org/10.3390/ma14081875.
[56] J. Carrey, B. Mehdaoui, M. Respaud, Simple models for dynamic hysteresis loop calculations of magnetic single-domain nanoparticles: application to magnetic hyperthermia optimization, J. Appl. Phys. 109 (2011), 083921, https://doi.org/10.1063/1.3551582.
[57] O.M. Lemine, A. Alanazi, E.L. Albert, M. Hjiri, M.O. M'hamed, S.A. Alrub, A. Alkaoud, C.A.C. Abdullah, γ-Fe_2O_3/Gd_2O_3-chitosan magnetic nanocomposite for hyperthermia application: structural, magnetic, heating efficiency and cytotoxicity studies, Appl. Phys. A 126 (2020), 471, https://doi.org/10.1007/s00339-020-03649-5.
[58] B. Aslibeiki, N. Eskandarzadeh, H. Jalili, A. Ghotbi Varzaneh, P. Kameli, I. Orue, V. Chernenko, A. Hajalilou, L.P. Ferreira, M.M. Cruz, Magnetic hyperthermia properties of $CoFe_2O_4$ nanoparticles: effect of polymer coating and interparticle interactions, Ceram. Int. 48 (2022) 27995–28005, https://doi.org/10.1016/j.ceramint.2022.06.104.
[59] A.E. Deatsch, B.A. Evans, Heating efficiency in magnetic nanoparticle hyperthermia, J. Magn. Magn. Mater. 354 (2014) 163–172, https://doi.org/10.1016/j.jmmm.2013.11.006.
[60] J.-w Kim, J. Wang, H. Kim, S. Bae, Concentration-dependent oscillation of specific loss power in magnetic nanofluid hyperthermia, Sci. Rep. 11 (2021) 1–10, https://doi.org/10.1038/s41598-020-79871-1.